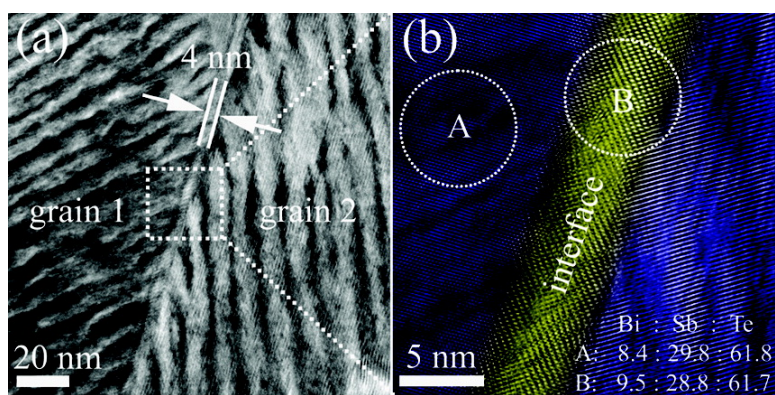


Structure Study of Bulk Nanograined Thermoelectric Bismuth Antimony Telluride

Yucheng Lan, Bed Poudel, Yi Ma, Dezhi Wang, Mildred S. Dresselhaus, Gang Chen, and Zhifeng Ren

Nano Lett., **2009**, 9 (4), 1419-1422 • DOI: 10.1021/nl803235n • Publication Date (Web): 25 February 2009

Downloaded from <http://pubs.acs.org> on April 8, 2009



More About This Article

Additional resources and features associated with this article are available within the HTML version:

- Supporting Information
- Access to high resolution figures
- Links to articles and content related to this article
- Copyright permission to reproduce figures and/or text from this article

[View the Full Text HTML](#)



ACS Publications
High quality. High impact.

Structure Study of Bulk Nanograined Thermoelectric Bismuth Antimony Telluride

Yucheng Lan,[†] Bed Poudel,[‡] Yi Ma,^{†,‡} Dezhi Wang,[†] Mildred S. Dresselhaus,[§]
Gang Chen,^{*,||} and Zhifeng Ren^{*,†}

Department of Physics, Boston College, Chestnut Hill, Massachusetts 02467, GMZ Energy, Inc., 12A Hawthorn Street, Newton, Massachusetts 02458, and Department of Physics, Department of Electrical Engineering and Computer Science, Department of Mechanical Engineering, Massachusetts Institute of Technology, Cambridge, Massachusetts 02139

Received October 26, 2008; Revised Manuscript Received January 2, 2009

ABSTRACT

The microstructures of bulk nanograined *p*-type bismuth antimony telluride with a thermoelectric dimensionless figure-of-merit $ZT = 1.4$ are investigated using transmission electron microscopy. It is found that the bulk material contains both nano- and micro-sized grains. Between the nanograins, bismuth-rich interface regions with a 4 nm thickness were detected. In addition, nanoprecipitates as well as other defects are also found to be embedded in the nanograins. The high ZT is attributed to the slight increase in the electrical conductivity, and to the large decrease of the thermal conductivity.

Since the 1950s, thermoelectric materials that convert electrical energy into thermal energy or vice versa have been used in cooling, refrigeration, and power generation.^{1–3} The effectiveness of a thermoelectric material is related to its dimensionless thermoelectric figure-of-merit $ZT = (S^2\sigma/k)T$, where S , σ , k , and T are the Seebeck coefficient, electrical conductivity, thermal conductivity, and absolute temperature, respectively.¹ Up to now, reasonably high ZT values have been achieved in either single crystalline bulk ingots^{4,5} or superlattices^{6–8} and nanostructured bulk materials.^{9–11} The significant enhancement of ZT from 1 in the commercial ingot to 1.4 in the nanograined bulk bismuth antimony telluride ($\text{Bi}_x\text{Sb}_{2-x}\text{Te}_3$) alloy,^{10,11} as the result of the reduction in thermal conductivity and the increase in electrical conductivity, is closely related to the unique microstructures of the nanograined bulk material. This work reports a detailed study of microstructures and elemental microanalysis of such nanograined bulk materials. Throughout the paper, only a qualitative correlation between the microstructure and thermoelectric properties is presented. A quantitative analysis is much more difficult at this stage. The structural information

obtained from these investigations will contribute in a major way to guiding modeling of the scattering processes determining the calculation of the thermal conductivity of nanograined BiSbTe composite materials with an eye toward further improvement of the materials processing of the nanocomposites and leading to further increases in ZT .

Experimental Section. The nanograined bulk $\text{Bi}_x\text{Sb}_{2-x}\text{Te}_3$ was prepared by a ball milling and hot-press method.^{10,11} TEM specimens were prepared from the nanograined bulk $\text{Bi}_x\text{Sb}_{2-x}\text{Te}_3$ by dicing, mechanical polishing, and Ar^+ -ion milling. The microstructures were investigated using a JEOL-2010F transmission electron microscope (TEM) operated at 200 kV. The microstructures of the crystalline ingot were also studied for comparison. For the statistics of grain and precipitate size, only those particles neighboring more than two other particles are counted as grains. All other particles embedded in grains or located between two grains are considered as precipitates. The area of each grain or precipitate was measured and converted into a maximum cross-sectional area of an equivalent sphere.

Results and Discussion. Figure 1a is a typical bright-field TEM (BF-TEM) image of four grains in the nanograined bulk material. No cavity between grains is observed, consistent with the 100% density of the nanograined bulk material. Usually the grains are polygonal. Selected area electron diffraction shows that the grains are single crystals with random orientations. Figure 1b shows a high-resolution

* To whom correspondence should be addressed. E-mail: (G.C.) gchen2@mit.edu; (Z.F.R.) renzh@bc.edu.

[†] Boston College.

[‡] GMZ Energy, Inc.

[§] Department of Physics and Department of Electrical Engineering and Computer Science, Massachusetts Institute of Technology.

^{||} Department of Mechanical Engineering, Massachusetts Institute of Technology.

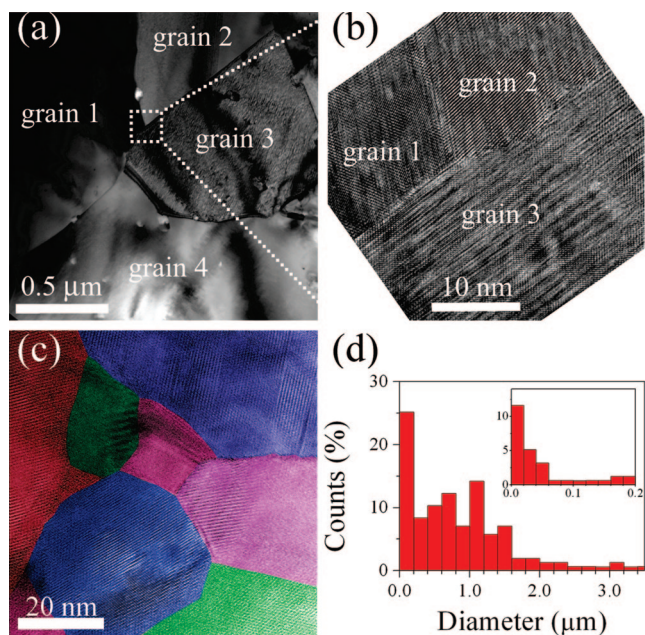


Figure 1. (a) BF-TEM image of multigrains, (b) HRTEM of grain boundaries, (c) HRTEM images of smaller grains, and (d) particle size distribution histogram for the nanogained bulk material with the inset zooming in on the distribution of small size particles less than 200 nm.

TEM (HRTEM) image of grain boundaries between three adjacent grains. The high-angle grain boundaries are well crystallized and free of second phase material. The randomness of the crystalline orientation of the adjacent grains promotes phonon scattering significantly. Figure 1c shows an HRTEM image of smaller grains. These small grains are also single crystals and are closely packed, similar to the bigger grains shown in Figure 1a.

Figure 1d shows the grain size distribution. Clearly, the majority of the grains are of diameters below $1.6 \mu\text{m}$. The inset of Figure 1d shows that 12% of the grains have a diameter less than 20 nm and 5% have a diameter in the 20–40 nm range. The grain boundaries scatter phonons with mean free paths comparable to the grain size, thereby reducing the thermal conductivity. The wide grain size distribution shown in Figure 1d is responsible for scattering phonons with a variety of wavelengths. Small particles embedded in larger particles also provide effective phonon scattering centers, as discussed below.

In addition to the clean boundaries between grains, as shown in Figure 1a–c, about 50% of the grains in the nanogained bulk material are surrounded by nanometer thick interface regions. Figure 2 shows images of such an interface region, 4 nm thick, in high resolution (Figure 2a) and in the lattice image mode (Figure 2b), respectively. The energy dispersive X-ray spectrum (EDS) indicates that the interface region is slightly bismuth-rich (1.1 ± 0.5 atomic % higher than that of the grains). These excess Bi atoms can be in the form of Bi antisite atoms, that is, Bi replacing Te, which creates a hole carrier.¹² Meanwhile, the excess Bi at the interface suggests a deficiency of Bi inside the grain, which could be in the form of a Bi vacancy or Te replacing the Bi, the so call Te antisite.¹³ It is known that a Bi vacancy donates

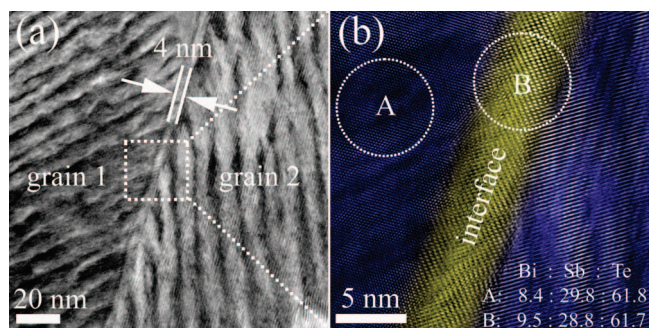


Figure 2. (a) TEM and (b) HRTEM image of a bismuth-rich interface region between two grains in the nanogained bulk material. The dotted circles indicate the regions from where EDS spectra were measured (with the compositions for each region given in atomic percentage).

three holes while a Te antisite creates an electron.¹² Our sample has a higher hole concentration than the parent crystalline ingot material, which could be due to the Bi vacancies inside the grain, while the grain boundary region may have even more holes, creating an electrostatic potential that preferentially scatters electrons. The increased hole concentration increases the electrical conductivity, while at the same time reducing the bipolar contribution to the electronic thermal conductivity at high temperatures. Our model¹⁰ also suggests that the interfacial potential barrier preferentially scatters electrons that further reduce the bipolar thermal conductivity, hence leading to a higher electronic power factor at higher temperatures, while at the same time the interfacial potential barrier scatters phonons.

There are many three-dimensional nanoprecipitates either embedded in the grains or located at the grain boundaries. In the experiments, four kinds of nanoprecipitates in the nanogained bulk material are observed, and these are shown in Figure 3a–d, respectively. One kind is a nanoprecipitate without boundaries (Figure 3a). No obvious lattice distortion is here seen between the grain matrix and the nanoprecipitate. The nanoprecipitates in the image are brighter than the surrounding crystalline grain matrix. EDS (curve a in Figure 3e) shows that the nanoprecipitate is antimony-rich and tellurium-poor. The second type of nanoprecipitate, as shown in Figure 3b, is a nanodot with twisted boundaries relative to the surrounding material. The chemical composition of the nanodots is the same as the surrounding matrix. The third type of nanoprecipitate, as shown in Figure 3c, also has a twisted grain boundary but is antimony-rich. The EDS of such an Sb-rich nanoprecipitate is plotted as curve c in Figure 3e. Because Sb has similar chemical characteristics as Bi, these Sb-rich regions may play a similar role as the Birich grain boundary region in terms of carrier transport. The fourth type of nanoprecipitate is a pure tellurium nanodot, shown in Figure 3d. The EDS of such a precipitate is plotted as curve d in Figure 3e. The pure tellurium precipitates are polygonal in shape with sharp grain boundaries while the other three kinds of precipitates show irregular more diffuse boundaries. We do not know the electronic characteristics of such Te nanodots embedded in the matrix. However, the Te precipitates suggest that in other regions, there are more Bi or Sb antisites, which create holes.

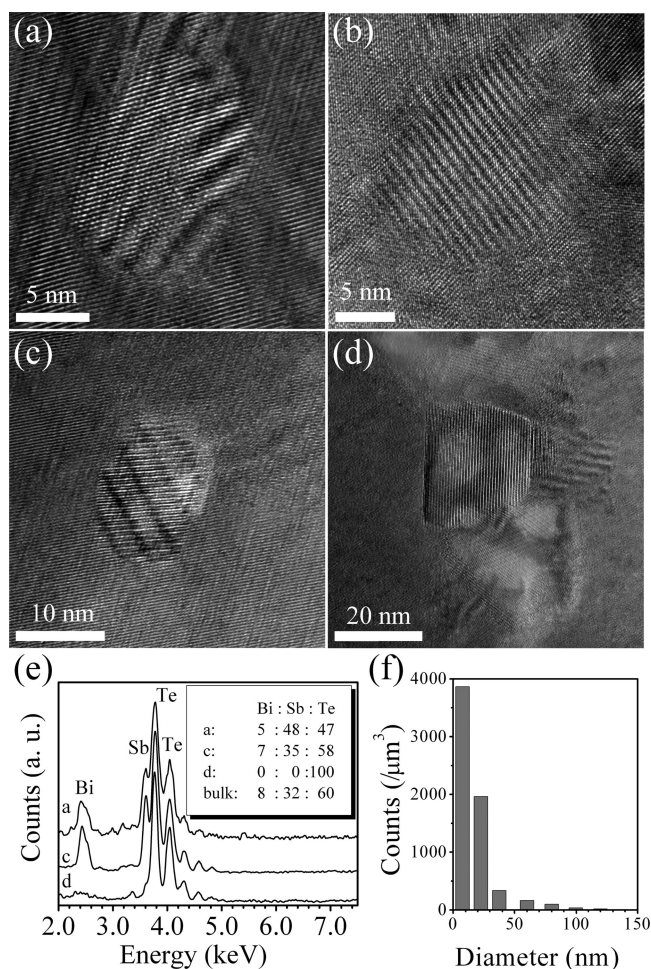


Figure 3. HRTEM images of nanoprecipitates embedded in the grain matrix. (a) An antimony-rich precipitate without a boundary, (b) a precipitate with a twisted boundary but with the same composition as the surrounding matrix, (c) an antimony-rich precipitate with a twisted boundary, (d) a tellurium precipitate with a high-angle boundary, (e) EDS spectra of the precipitates in panels a–d with the composition of each given in atomic percentage, as shown in the inset, and (f) precipitate size distribution.

Hall effect measurements at room temperature confirm the fact that the hole carrier concentration ($n = 2.5 \times 10^{19}/\text{cm}^3$) of the nanograined bulk material is about 39% higher than that of the ingot ($n = 1.8 \times 10^{19}/\text{cm}^3$). According to the equation $\sigma = ne\mu$, where μ is the carrier mobility measured from the Hall effect, the 39% higher carrier concentration increases the electrical conductivity of the nanograined bulk material by 27% due to a decrease of the mobility from $298 \text{ cm}^2/\text{Vsec}$ to $264 \text{ cm}^2/\text{Vsec}$, in good agreement with the four-probe measurements of the electrical conductivity (25% higher for the nanograined bulk material than that of the ingot¹⁰).

Figure 3f is a diameter distribution histogram for all of these precipitates collectively. The precipitate concentration in the nanostructured bulk material increases rapidly with decreasing precipitate size. Even though the volume of these nanoprecipitates accounts for only $\sim 5\%$ of the nanograined bulk material, there is a lot of surface area to scatter short wavelength phonons. Besides increasing the carrier concentration, the nanoprecipitates within almost every grain scatter

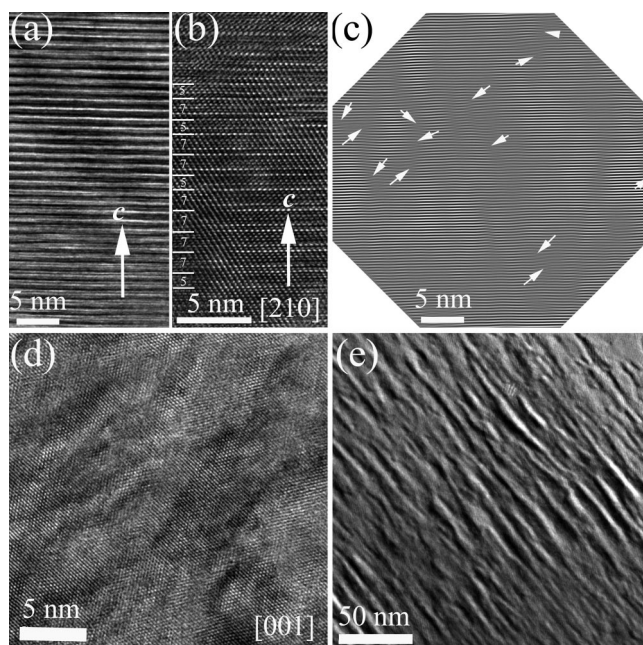


Figure 4. HRTEM images of precipitate-free regions in grains (a) with excited $\{003\}$ reflections, (b) along the $[210]$ zone (Numbers 5 and 7 represent 5- and 7-layer lamellae, respectively), (c) with excited $\{105\}$ reflections (Wiener-filtered) (white arrows indicate threading dislocations), (d) along the $[001]$ zone, and (e) TEM image of structural modulations.

phonons, especially phonons with mean free paths matched with the precipitate size, thus greatly reducing contributions to the lattice thermal conductivity over the wide range of phonon mean free paths present in these thermoelectric materials.

Besides precipitates, there are other kinds of defects in the nanograins of the bulk material. Figure 4a is an HRTEM image showing lattice stripes of various widths. Figure 4b shows an HRTEM image of these stripes along the $[210]$ zone. A series of two rows of extra-bright dots sandwiching a row of weaker bright dots are separated by two or four weaker bright dot-rows, forming five-layer or seven-layer lamellae. Five-layer lamellae represent the ideal structure of Bi_2Te_3 with a stacking of $-\text{Te}-\text{Bi}-\text{Te}-\text{Bi}-\text{Te}$ ¹⁴ while seven-layer lamellae represent a common structure of $\text{Bi}_{2+\delta}\text{Te}_3$.¹⁵ In the nanograins, the five-layer and seven-layer lamellae stack randomly along the c -axis. Such stacking faults would also scatter phonons and decrease the thermal conductivity.

Figure 4c shows threading dislocations in the precipitate-free regions of the grains. The dislocation concentration here is $\sim 10^{11}/\text{cm}^2$, at least ten times higher than $\sim 5 \times 10^9/\text{cm}^2$ found in the crystalline ingot. Numerous point defects are observed in the grains of the nanograined bulk material, as shown in Figure 4d. The point defect concentration is 2–3 orders of magnitude higher than that of the ingot. Figure 4e shows the structural modulations in the grains. No big difference in the modulations is observed between the nanograined bulk material and the ingot. All these low-dimensional defects (point defects, dislocations, and structural modulations) are common properties of both the nanograined bulk material and the ingot, as observed in both undoped- Bi_2Te_3 and doped Bi_2Te_3 alloys.^{16,17} However, the defect

concentrations in the nanograined bulk material are much higher than those in the ingot. The defects with higher concentrations would scatter phonons more effectively and further decrease the thermal conductivity of the nanograined bulk material.

Although quantitatively identifying different contributions of the nanostructures to the transport properties is not possible at this stage, we believe that the nanostructures and imperfections scatter all phonons with mean free paths from the micron scale down to the atomic scale, thus greatly reducing the thermal conductivity. Bismuth-rich interface regions and nanoprecipitates contribute to the hole concentration, and may also create interfacial barriers that preferentially scatter electrons, both effects leading to a reduction in the bipolar electronic thermal conductivity. As a result, compared with the ingot, the thermal conductivity at room temperature of the nanograined bulk material decreases by 20% and the electrical conductivity at room temperature increases by 25%. The peak ZT is increased by 40% at 100 °C. However, at 250 °C the improvement in ZT compared to bulk crystalline material is about 200%, due to a reduced bipolar contribution to both the electronic thermal conductivity and the Seebeck coefficient, as well as reduced phonon thermal conductivity. One fact that should be mentioned is that the interface regions and nanoprecipitates induce a 25% increase in the electrical conductivity while their volume only accounts for about 6.3% (5% for nanoprecipitates and 1.3% for interface regions) of the whole nanograined bulk material.

Conclusions. In summary, we have performed a detailed analysis of the microstructures of p-type nanograined bulk bismuth antimony telluride with a peak ZT of 1.4 at 100 °C. The microstructural analysis suggests that the nanograined bulk material consists of grains with diameters distributed from a few nanometers to about 2 μm , which helps to scatter phonons over the corresponding range of wavelengths and mean free paths. Nearly 50% of the nanograins are separated by bismuth-rich nanointerface regions. Nanoprecipitates are embedded within the grains or are located at the grain boundaries. The defect concentrations in the nanograined bulk material are much higher than those of the ingot. These unique microstructures enhance the hole concentration, which leads to an increased electrical conductivity and a reduced bipolar contribution to the electronic thermal conductivity and the Seebeck coefficient, while simultaneously decreasing the phonon thermal con-

ductivity efficiently, resulting in a higher ZT overall of the nanograined bulk material. The structural information obtained from these investigations will contribute in a major way to guiding the modeling of the scattering processes that enter into the calculation of the thermal conductivity of nanograined BiSbTe composite materials, with an eye toward further improvement of the materials processing of the nanocomposites and thereby leading to further increases in ZT.

Acknowledgment. The work is sponsored by DOE DE-FG02-00ER45805 (Z.F.R.), DOE DE-FG02-02ER45977 (G.C.), NSF NIRT 0506830 (G.C., Z.F.R., and M.D.), NSF CMMI 0833084 (Z.F.R. and G.C.), and DOE DE-FG02-08ER46516 (M.D., G.C., and Z.F.R.).

Note Added after ASAP Publication: This paper was published ASAP on February 25, 2009. A grant number in the Acknowledgment was changed. The revised paper was reposted on March 10, 2009.

References

- (1) Goldsmid, H. J. *Thermoelectric Refrigeration*; Plenum Press, New York, 1964.
- (2) Wood, C. *Rep. Prog. Phys.* **1988**, *51*, 459.
- (3) Dresselhaus, M. S.; Chen, G.; Tang, M. Y.; Yang, R. G.; Lee, H.; Wang, D. Z.; Ren, Z. F.; Fleurial, J. P.; Gogna, P. *Adv. Mater.* **2007**, *19*, 1043.
- (4) Morelli, T.; Caillat, T.; Fleurial, J. P.; Borshchevsky, A.; Vandersande, J.; Chen, B.; Uher, C. *Phys. Rev. B* **1995**, *51*, 9622.
- (5) Caillat, T.; Borshchevsky, A.; Fleurial, J. P. *J. Appl. Phys.* **1996**, *80*, 4442.
- (6) Hicks, L. D.; Harman, T. C.; Sun, X.; Dresselhaus, M. S. *Phys. Rev. B* **1996**, *53*, R10493.
- (7) Venkatasubramanian, R.; Siivola, E.; Colpitts, T.; O'Quinn, B. *Nature* **2001**, *413*, 597.
- (8) Harman, T. C.; Taylor, P. J.; Walsh, M. P.; LaForge, B. E. *Science* **2002**, *297*, 2229.
- (9) Hsu, K. F.; Loo, S.; Guo, F.; Chen, W.; Dyck, J. S.; Uher, C.; Hogan, T.; Polychroniadis, E. K.; Kanatzidis, M. G. *Science* **2004**, *303*, 818.
- (10) Poudel, B.; Hao, Q.; Ma, Y.; Lan, Y. C.; Minnich, A.; Yu, B.; Yan, X.; Wang, D. Z.; Muto, A.; Vashae, D.; Chen, X. Y.; Liu, J. M.; Dresselhaus, M. S.; Chen, G.; Ren, Z. F. *Science* **2008**, *320*, 634.
- (11) Ma, Y.; Hao, Q.; Poudel, B.; Lan, Y. C.; Yu, B.; Wang, D. Z.; Chen, G.; Ren, Z. F. *Nano Lett.* **2008**, *8*, 2580.
- (12) Pecheur, P.; Toussaint, G. *J. Phys. Chem. Solids* **1994**, *35*, 327.
- (13) Horak, J.; Cermak, K.; Koudelka, L. *J. Phys. Chem. Solids* **1986**, *47*, 805.
- (14) Drabble, J.; Goodman, C. *J. Phys. Chem. Solids* **1958**, *5*, 142.
- (15) Frangis, N.; Kuypers, S.; Manolikas, C.; Landuyt, J. V.; Amelinckx, S. *Solid State Commun.* **1989**, *69*, 817.
- (16) Peranio, N.; Eibl, O.; Nurnus, J. *J. Appl. Phys.* **2006**, *100*, 114306.
- (17) Maier, D. *Solid State Commun.* **2002**, *122*, 565.

NL803235N